JOURNAL OF GEOPHYSICAL RESEARCH, VOL. 117, A08223, doi:10.1029/2011JA017358, 2012

Hybrid simulation of the shock wave trailing the Moon

P. Israelevich[1] and L. Ofman[1,2,3]

Received 10 November 2011; revised 7 July 2012; accepted 10 July 2012; published 25 August 2012.

[1] A standing shock wave behind the Moon was predicted by Michel (1967) but never observed nor simulated. We use 1D hybrid code in order to simulate the collapse of the plasma-free cavity behind the Moon and for the first time to model the formation of this shock. Starting immediately downstream of the obstacle we consider the evolution of plasma expansion into the cavity in the frame of reference moving along with the solar wind. Well-known effects as electric charging of the cavity affecting the plasma flow and counterstreaming ion beams in the wake are reproduced. Near the apex of the inner Mach cone where the plasma flows from the opposite sides of the obstacle meet, a shock wave arises. We expect the shock to be produced at periods of high electron temperature solar wind streams ($T_i \ll T_e \sim 100$ eV). The shock is produced by the interaction of oppositely directed proton beams in the plane containing solar wind velocity and interplanetary magnetic field vectors. In the direction across the magnetic field and the solar wind velocity, the shock results from the interaction of the plasma flow with the region of the enhanced magnetic field inside the cavity that plays the role of the magnetic barrier. The appearance of the standing shock wave is expected at the distance of $\sim 7R_M$ downstream of the Moon.

Citation: Israelevich, P., and L. Ofman (2012), Hybrid simulation of the shock wave trailing the Moon, *J. Geophys. Res.*, *117*, A08223, doi:10.1029/2011JA017358.

1. Introduction

[2] An idealized picture of the interaction between supersonic and super-Alfvénic solar wind flow and non-magnetized celestial bodies without an atmosphere such as the Moon, asteroids, etc. (see Figure 1) can be outlined as follows [e.g., *Michel*, 1968]. The solar wind particles are absorbed by the surface when they impact the celestial body whereas the velocity of the bypassing particles remains unchanged. As a result, a cavity free of solar wind plasma is formed behind the obstacle. Because of thermal dispersion of velocities of the impacting particles population, some of the particles behind the limb have a velocity component directed toward the axis of symmetry of the cavity. These particles penetrate the geometric shadow of the celestial body. Since the bulk velocity of the solar wind is larger than the thermal velocity, the depth of penetration is proportional to the distance from the limb and the cavity free of plasma takes a conical shape. Considering the frame of reference moving with the solar wind velocity, the process of refilling of the region of geometrical shadow with plasma is equivalent to the plasma expansion in vacuum [*Samir et al.*, 1983]. Since the thermal velocity of electrons is much higher than the solar wind speed therefore, at the very initial stage fast electrons enter the whole region of the geometrical shadow charging it negatively. As soon as the negative potential reaches $\sim T_e/e$ (where T_e is the electron temperature) further charge separation stops, and electrons continue to fill the cavity along with solar protons that are accelerated by the negative potential in the cavity to the ion-acoustic velocity $c_s \sim \sqrt{\frac{T_e}{M}}$. The cavity is restricted by the inner Mach cone of the angle $\tan \beta = c_s/v_{sw}$, where v_{sw} is the solar wind speed [*Michel*, 1968]. Plasma expansion into the cavity is accompanied by rarefaction wave propagation away from the cavity axis. Since the solar wind is supersonic the outer Mach cone restricts the region occupied by the rarefaction wave and the solar wind plasma flow outside this cone remains unperturbed.

[3] The presence of the interplanetary magnetic field (IMF) introduces asymmetry in this description. If we consider the coordinate system with X-axis along the solar wind outflow velocity and Y-axis defined in a way that the IMF vector lays in the XY-plane, the plasma flow along the magnetic field fills the cavity. If the B_x-component of the magnetic field is present and the magnetic field lines are inclined to the Y-axis at an angle $\alpha = \arctan(B_x/B_y)$, then the bulk plasma velocity directed toward the wake axis is different at the opposite sides of the wake as shown by vector diagrams in Figure 1. The inner Mach cone is not

[1]Department of Geophysics and Planetary Sciences, Raymond and Beverly Sackler Faculty of Exact Sciences, Tel Aviv University, Ramat Aviv, Israel.
[2]Department of Physics, Catholic University of America, Washington, DC, USA.
[3]NASA Goddard Space Flight Center, Greenbelt, Maryland, USA.

Corresponding author: P. Israelevich, Department of Geophysics and Planetary Sciences, Raymond and Beverly Sackler Faculty of Exact Sciences, Tel Aviv University, Ramat Aviv 69978, Israel. (peter@post.tau.ac.il)

0148-0227/12/2011JA017358

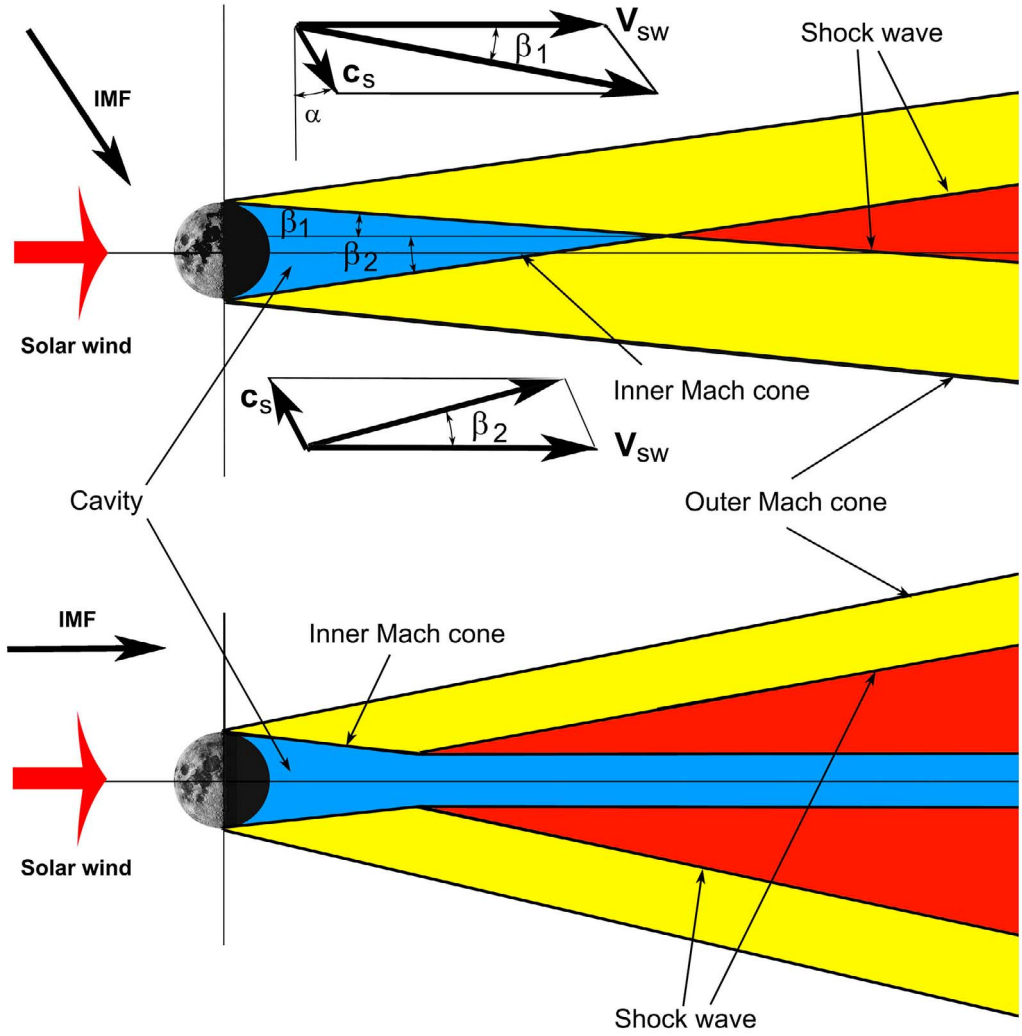

Figure 1. A diagram showing the formation of the lunar wake. The arrows show the directions of the solar wind velocity and the interplanetary magnetic field (IMF). Thick solid lines show the positions of the boundaries, blue, yellow and red colors correspond to the cavity free of plasma, rarefaction region and the region of enhanced plasma density, respectively. Vector diagrams explain the plasma entrance into the cavity from two opposite sides. Bottom panel shows the wake structure for the case when the IMF is aligned along the solar wind velocity.

symmetric: the angles at the apex of the cone are not equal $\beta_1 \neq \beta_2$. Simple geometric consideration shows that $\tan \beta_{1,2} = \dfrac{c_s \cos\alpha}{v_{sw} \pm c_s \sin \alpha}$, and the length of the cavity is $L = 2R_M \dfrac{M_s^2 - \sin^2\alpha}{M_s \cos \alpha}$, where R_M is the Moon radius and $M_s = v_{sw}/c_s$ is the Mach number. For the case $B_x = 0$, $L = 2R_M M_s$. The cavity length doubles for $\alpha = 60°$ and grows rapidly with further increase of α. For case of IMF parallel to the solar wind velocity ($\alpha = 90°$), the cavity becomes an infinite cylinder as shown in the bottom panel of Figure 1.

[4] Across the magnetic field in the Z direction, plasma moves along with the frozen-in magnetic field lines. This flow results in magnetic field compression inside the cavity and magnetic field decrease in the rarefaction region between the inner and outer Mach cones.

[5] These main features of the solar wind interaction with the Moon were observed in the very first measurements by Explorer 35 satellite [*Colburn et al.*, 1967; *Lyon et al.*, 1967; *Ness et al.*, 1967] and later confirmed by the Wind [*Ogilvie et al.*, 1996; *Owen et al.*, 1996; *Bosqued et al.*, 1996], LRO [*Halekas et al.*, 2005], Kaguya [*Nishino et al.*, 2009], and Artemis [*Halekas et al.*, 2011] spacecraft. They were reproduced in laboratory experiments as well [*Kristoferson*, 1969; *Podgorny and Andrijanov*, 1978; *Podgorny et al.*, 1980], and in numerical simulations [*Lipatov* 1976, 2002; *Farrell et al.*, 1998; *Birch and Chapman*, 2001; *Kallio* 2005; *Kimura and Nakagawa*, 2008; *Lipatov et al.*, 2011; *Wang et al.*, 2011, *Wiehle et al.*, 2011; *Holmström et al.*, 2012].

[6] However, there is another feature expected for the solar wind interaction with the Moon that was not observed or modeled yet. *Michel* [1967, 1968] pointed out that a consequence of solar plasma flow into the cavity would be the appearance of a shock wave at the place where the collapse of the cavity is halted. The orbits of previous near-

Moon spacecrafts were too low in order to reach the region of expected shock and it was not observed experimentally.

[7] One of the possible explanations why the shock wave was not observed in past numerical simulations is as follows. The typical electron temperature used in these simulations was $T_e \sim T_i \sim 10$ eV [*Lipatov* 1976, 2002; *Farrell et al.*, 1998; *Birch and Chapman*, 2001; *Kallio* 2005; *Kimura and Nakagawa*, 2008; *Lipatov et al.*, 2011; *Wang et al.*, 2011, *Wiehle et al.*, 2011; *Holmström et al.*, 2012]. In the present study, we model for the first time the formation of this shock for the case $T_e \gg T_i$ in hot solar wind streams ($T_e \sim 100$ eV) using 1D hybrid code.

[8] Near the apex of the inner Mach cone two opposing flows of plasma meet and their relative velocity is approximately $2c_s$. Therefore it is natural to expect that a standing shock will arise at this location as shown in Figure 1. In case of the magnetic field parallel to the solar wind flow (the cavity is not collapsed as shown in the bottom panel of Figure 1) the standing shock wave may still exist. If the transition from collapsing cavity to a region of enhanced magnetic field with constant cross-section occurs as discontinuous change in local physical quantities then the appearance for the shock wave is evident. A smoothing out of the transition between the two limiting shapes does not eliminate the shock wave except in the immediate vicinity of the boundary where it becomes a weak discontinuity that evolves in a shock wave [*Michel*, 1968; *Wolf*, 1968]. In this paper, we perform for the first time hybrid numerical simulation of the shock wave formation behind the Moon.

2. Model

[9] We follow the simple method used by *Farrell et al.* [1998] and *Birch and Chapman* [2001]. Let us consider the frame of reference moving along the *X*-axis with the solar wind velocity v_{sw}. In this frame, the solar wind plasma expands into the plasma-free region with initial shape corresponding to the cross-section of the obstacle. Solution of the time-dependent 2D fluid problem is $f(t, y, z)$. Making the substitution $x = v_{sw}t$, one returns to the obstacle frame of reference and obtains an approximate solution of the 3D problem of steady state flow around an obstacle $f(x, y, z)$. Similarly, 1D problem of plasma expansion in vacuum considered in this study yields the approximate solution $f(t, y) \rightarrow f(x, y)$ for 2D flow around an infinite plate of width $2y_0$ with an axis parallel to *Z*.

[10] We consider supersonic and super Alfvénic plasma flow around an infinite cylinder. The coordinate system is as follows: *X*-axis is along the solar wind velocity, *Z*-axis is parallel to the cylinder axis ($\partial/\partial z = 0$), and *Y*-axis completes the system. Solutions are obtained for two cases (a) expansion along the magnetic field ($\mathbf{B}_0 = (0, B_0, 0)$), and (b) expansion across the magnetic field ($\mathbf{B} = (0, 0, B_0)$).

[11] We use the 1D hybrid code, based on the code developed by *Winske and Omidi* [1993], and later modified by A. Viñas (private communication, 1995) and *Ofman et al.* [2001, 2009]. In the hybrid model the ions are represented as particles, neglecting collisions, while the electrons are described as a finite temperature massless fluid that maintains the quasineutrality of the plasma. This numerical modeling method allows one to resolve the ion dynamics and to integrate the equations over many ion cyclotron periods, while neglecting the small temporal- and spatial-scales of the electron kinetic motions. In the hybrid model, the three components of order million particle velocities were used to calculate the currents, and the fields on the 1D grid. In our study the grid consisted of 512 cells, and the total length of our simulated region was $139c/\omega_p$, where ω_p is the plasma frequency, and c is the speed of light. The required number of particles per cell was determined by the required limitation on the overall statistical noise, and we have used up to 1600 particles per cell to reduce statistical noise to acceptable levels (i.e., the random noise in velocity space is much less than the thermal distribution). Note, that each numerical particle represents large number of real particles, with the conversion determined by the density normalization.

[12] The following equations of motion are solved for the ions:

$$\frac{d\mathbf{x}_i}{dt} = \mathbf{v}_i, \tag{1}$$

$$M\frac{d\mathbf{v}_i}{dt} = e\left(\mathbf{E} + \frac{\mathbf{v}_i \times \mathbf{B}}{c}\right), \tag{2}$$

where M is the proton mass and e is the electron charge. The electron momentum equation is solved by neglecting the electron inertia

$$\frac{\partial}{\partial t} n_e m_e \mathbf{v}_e = 0 = -en_e\left(\mathbf{E} + \frac{\mathbf{v}_e \times \mathbf{B}}{c}\right) - \nabla p_e, \tag{3}$$

where the electron pressure $p_e = n_e T_e$ is used for closure, and quasi-neutrality implies $n = n_e = n_i$, where n_k is the number density of electrons, and protons, respectively. Thus, the collisionless Ohm's law is obtained. We use the isothermal energy equation for electrons ($\gamma = 1$, $T = T_0 = Const.$), hence p_e is proportional to the number density n.

[13] The above equations are supplemented with Maxwell's equations $\nabla \times \mathbf{B} = \frac{4\pi}{c}\mathbf{J}$ and $\nabla \times \mathbf{E} = -\frac{1}{c}\frac{\partial \mathbf{B}}{\partial t}$. The field solutions are obtained on the 1D grid, and the particle (ion) equations of motions are solved as they respond to the fields at each time step. Three components of magnetic field and velocity vectors are included in the model. The numerical method has been tested and used successfully in many studies.

[14] The particle and field equations are integrated in time using the Rational Runge-Kutta (RRK) method [*Wambecq*, 1978], whereas the spatial derivatives are calculated by pseudospectral FFT method. The hybrid model allows computing the self-consistent evolution of the velocity distribution of the ions that includes the nonlinear effects of wave-particle interactions without additional assumptions. Moreover, the hybrid model is well suited to describe the nonlinear saturated state of the plasma.

[15] Typical parameters of the solar wind plasma at 1 AU are chosen as the initial condition: $n_0 = 5$ cm^{-3}, $B_0 = 10$ nT, $T_i = 5$ eV and the size of the obstacle $2y_0 = 3500$ km is the Moon's diameter.

[16] Since the necessary condition of ionacoustic instability development is $T_i \ll T_e$, we chose the electron temperature to be much higher than ion temperature: $T_e = 100$ eV. The

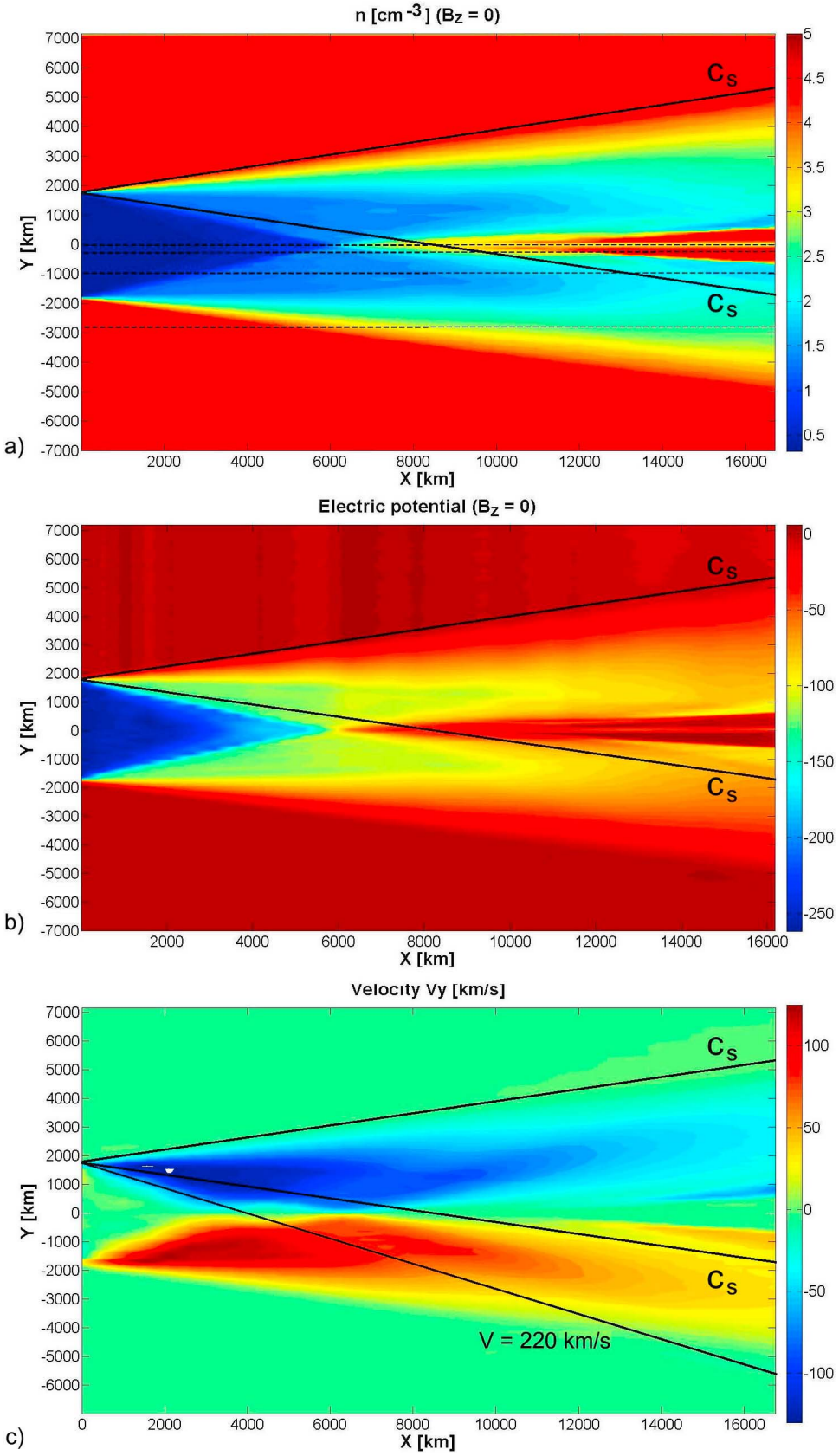

Figure 2. Distribution of the (a) number density, (b) electric potential, and (c) plasma velocity component V_y in the wake. Solid lines denote the plasma expansion with ion-acoustic velocity c_s. Expansion with V = 220 km/s is shown in Figure 2c.

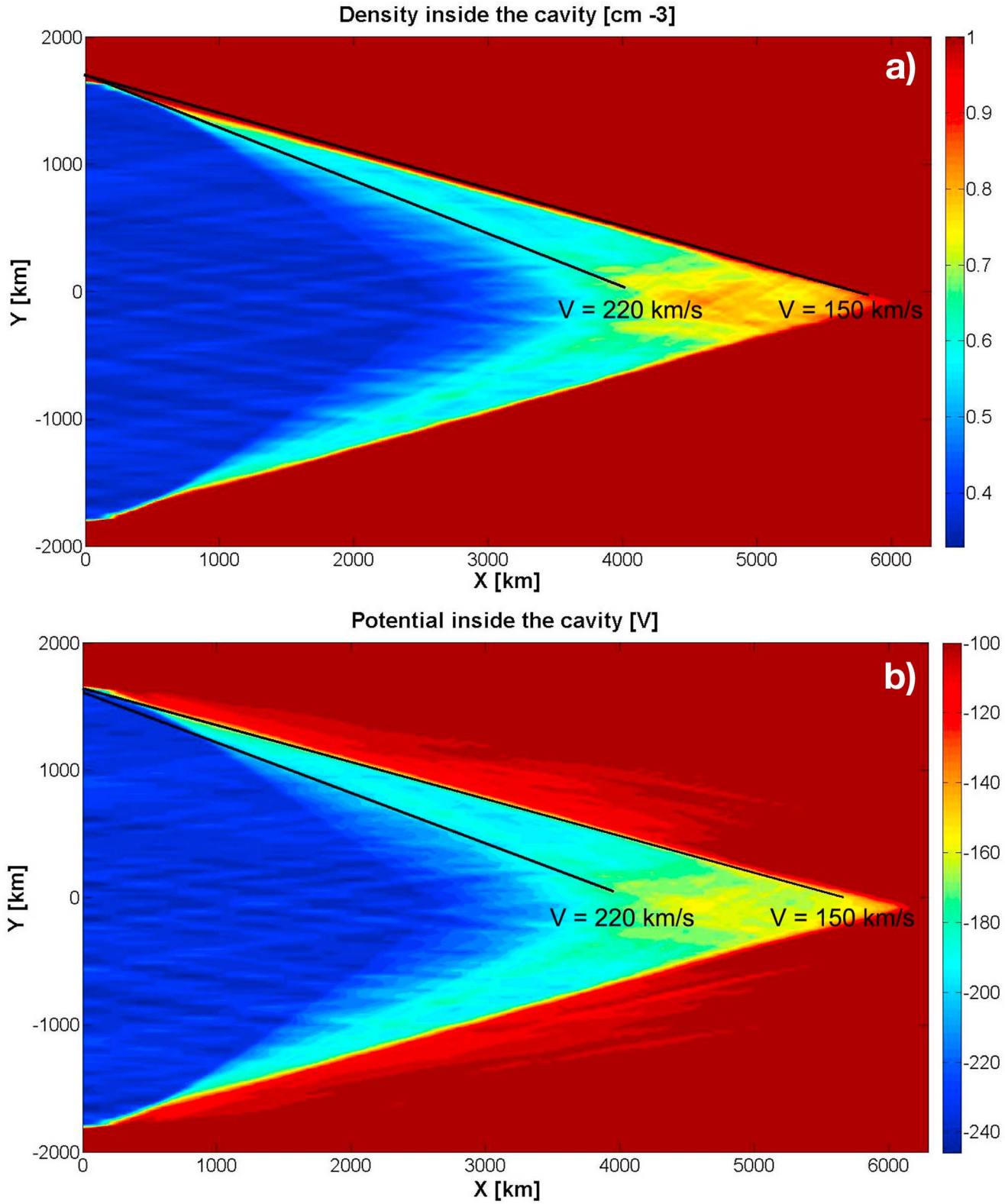

Figure 3. (a) Plasma density and (b) electric potential distribution inside the cavity. Solid lines show expansion with velocities V = 150 km/s (cavity boundary) and V = 220 km/s.

electron temperature in the solar wind can reach occasionally 40 eV [*Newbury et al.*, 1998]. Moreover, the solar wind electrons distribution function is not Maxwellian [see, e.g., *Feldman et al.*, 1975]. It rather consists from cold core electrons with the temperature $T_e \sim T_i \sim 10$ eV, and hotter halo (∼7%) with the temperature ∼50–100 eV. *Sittler and Burlaga* [1998] found that within solar wind magnetic clouds $T_e \gg T_i$, and $T_e / T_i \sim 7$, on average. Thus, our value of

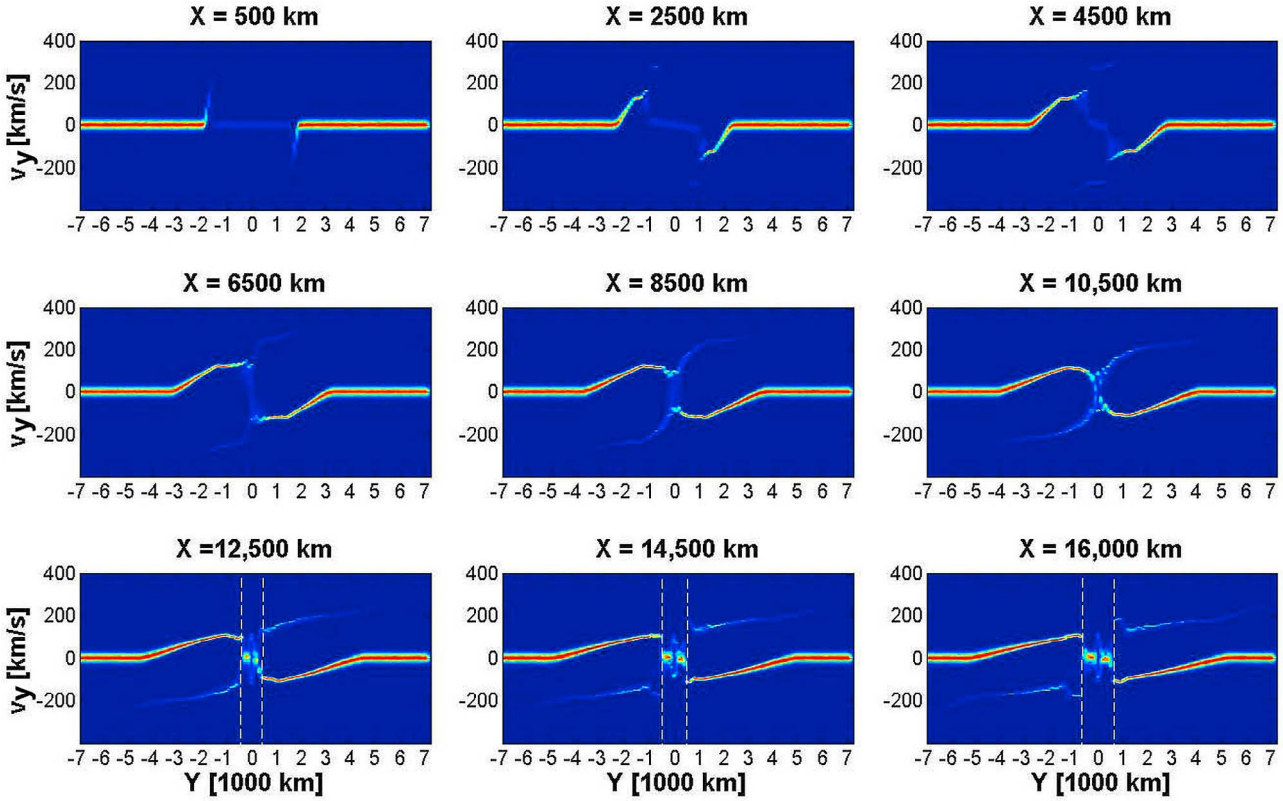

Figure 4. Distribution of protons in phase space ($y - v_y$) at 9 distances along the wake.

T_e represents the extreme conditions that guarantee the formation of the shock. However, we found that the shock can form at lower T_e as well (see below).

[17] The obstacle is centered at $y = 0$ at the time $t = 0$ (i.e., at the distance $x = 0$). The plasma density is n_0 for $|y| > y_0$, and $0.1n_0$ behind the obstacle for $|y| < y_0$ (zero density cannot be used for numerical reasons). All other parameters (velocity,

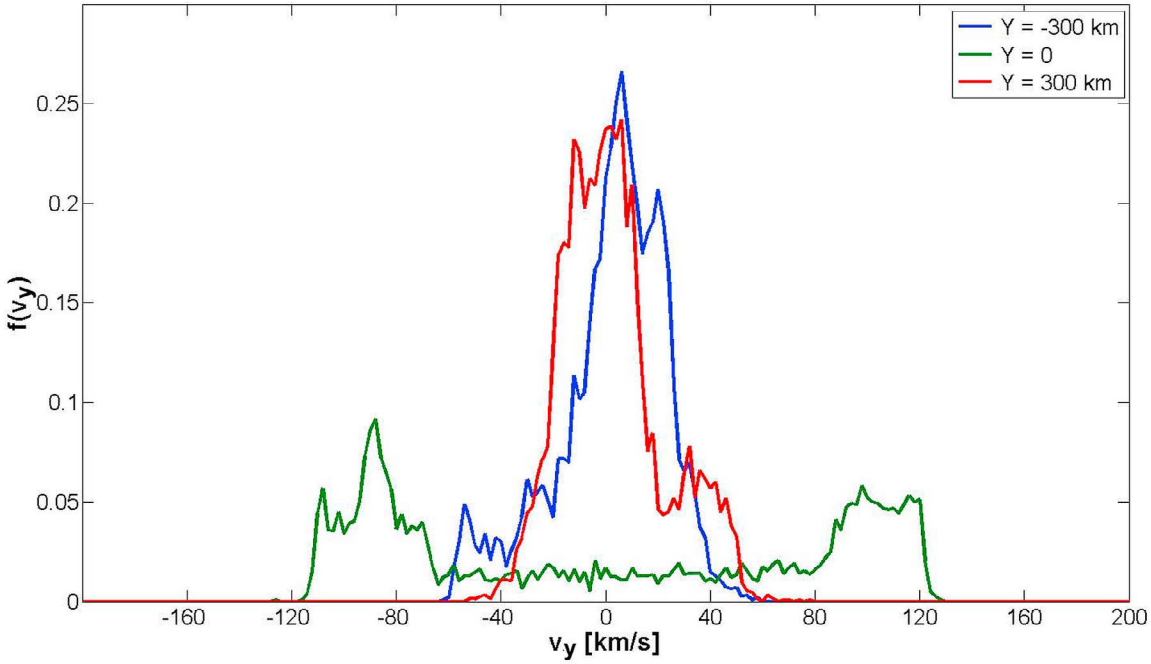

Figure 5. Proton velocity distribution functions at $X = 16{,}000$ km for $Y = -300$ km (blue), $Y = 0$ (green), and $Y = 300$ km (red line).

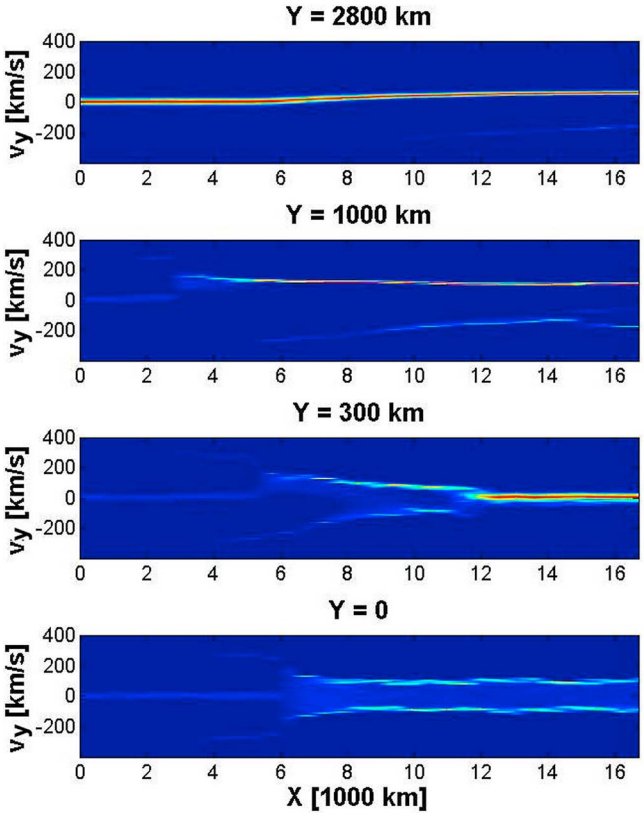

Figure 6. Dependencies of proton velocity distribution function on the distance in the wake X for the wake sections shown by dashed lines in Figure 2a. From top to bottom: $Y = 2800$ km, $Y = 1000$ km, $Y = 300$ km, and $Y = 0$.

temperature, magnetic field) are constant along the Y-axis at $t = 0$ ($x = 0$). The solar wind velocity $v_{sw} = 500$ km/s is not used explicitly in the simulations but serves for conversion of the time coordinate to the distance along the X-axis: $x = v_{sw}t$.

3. Results

3.1. Expansion Along the Magnetic Field ($B_x = B_z = 0$)

[18] Figure 2a shows the color-coded plasma density behind the obstacle. Simulation reproduces both the collapsing cavity and expanding rarefaction region restricted by the outer Mach cone. The cavity collapses at $X = 6000$ km. Starting from this distance, accumulation of plasma occurs near the center of the wake. The region of the enhanced plasma density expands with the distance reaching ~1500 km at $X = 16{,}000$ km. Rarefaction continues between the outer boundary of this region and outer Mach cone. Narrow (~300 km) minimum of the density is observed in the closest vicinity of the wake axis ($Y = 0$) starting from the distance of $X \sim 10{,}000$ km.

[19] For the neutral gas expansion in vacuum, the apex angles of the inner and outer Mach cones are the same and equal to $\tan\beta = V_s/V$ (where $V_s \sim \sqrt{\frac{T}{M}}$ and V are sound and flow velocities, respectively). Simulation shows that this is not the case for plasma expansion in vacuum. Thick solid lines in Figure 2a denote the inner and outer Mach cones for ion-acoustic velocity $\tan\beta = c_s/v_{sw}$ ($c_s = 98$ km/s). Figure 2a shows that the cavity collapse occurs with the velocity 145 km/s, which is higher than c_s. Rarefaction wave forming the outer Mach cone propagates with 88 km/s, i.e., slower than c_s. The asymmetry of perturbation propagation toward and away from the cavity is associated with the appearance of the electric field in the rarefaction region.

[20] Figure 2b shows the distribution of the electric potential in the wake of the obstacle. The potential is strongly negative inside the cavity reaching −260 V. This negative potential results from the strong gradient of the number density at the boundary of the cavity, as it follows from the Ohm's law (3): $n = n_0 \exp(e\varphi/T_e)$ or $\varphi = \ln n/n_0 \frac{T_e}{e}$.

[21] Figure 2c shows the distribution of the velocity component v_y. Solid lines correspond to the expansion with ion-acoustic velocity c_s and with the velocity $V = 220$ km/s. Thus, behind the solid body a conical region is formed (with the apex angle $\tan\alpha = V/v_{sw}$), where the number density remains the same as at the initial state. Outside this cone, protons are accelerated by the floating potential that appears inside the cavity. This results in the increase of the number density and the change of the electric potential. Further refill of the cavity occurs under the action of the electric potential at the boundary of the cavity.

[22] Figure 3 shows the density (Figure 3a) and the electric potential distribution (Figure 3b) inside the cavity. Due to the protons accelerated by the floating potential, the density inside the cavity (but outside the cone determined by the velocity $V = 220$ km/s) increases up to 0.8 cm^{-3}, and the negative potential at the cavity axis drops from −260 V to −180 V. Electric potential of the cavity boundary is $U_b = -120$ V, so the velocity of the cavity collapse should be $V = \sqrt{\frac{2eU_b}{M}} = 150$ km/s which is in good agreement with the simulation results.

[23] Evolution of the proton distribution in phase space (y,v_y) is shown in Figure 4. Each panel represents the dependence of the distribution function on Y (horizontal axes). Vertical axes are particle velocity component v_y and the number of particles within the velocity range $(v_y, v_y + dv_y)$ is color-coded (the distribution functions are normalized in such a way that $n = \int f(v)dv$). The results for t = 1 s, 5 s, 9 s, 13 s, 17 s, 21 s, 25 s, 29 s and 32 s (which correspond to the distances X along the flow direction of 500 km, 2500 km, 4500 km, 6500 km, 8500 km, 10,500 km, 12,500 km, 14,500 km and 16,000 km, respectively). The average velocity starts to increase at the outer Mach cone, and grows linearly till the boundary of the inner Mach cone. Inside the cavity the populations of protons accelerated by the floating potential to 240 km/s can be seen ($X = 2500$ and $X = 4500$ km). Starting at $X = 6500$ km two counterstreaming proton beams are observed near the axis of the wake ($Y = 0$). Also, the beams of high speed protons coming from the opposite sides of the obstacle can be seen in the rarefaction region starting from $X = 8500$ km. The proton beams in the rarefaction region practically do not interact with the ambient plasma streaming toward the wake axis and can be seen until the end of the simulation ($X = 16{,}000$ km). On the contrary, oppositely directed proton beams strongly interact in the vicinity of the axis. At $X = 8500$ km, two beams are clearly seen, whereas at $X = 10{,}500$ km the beam structure disappears and at

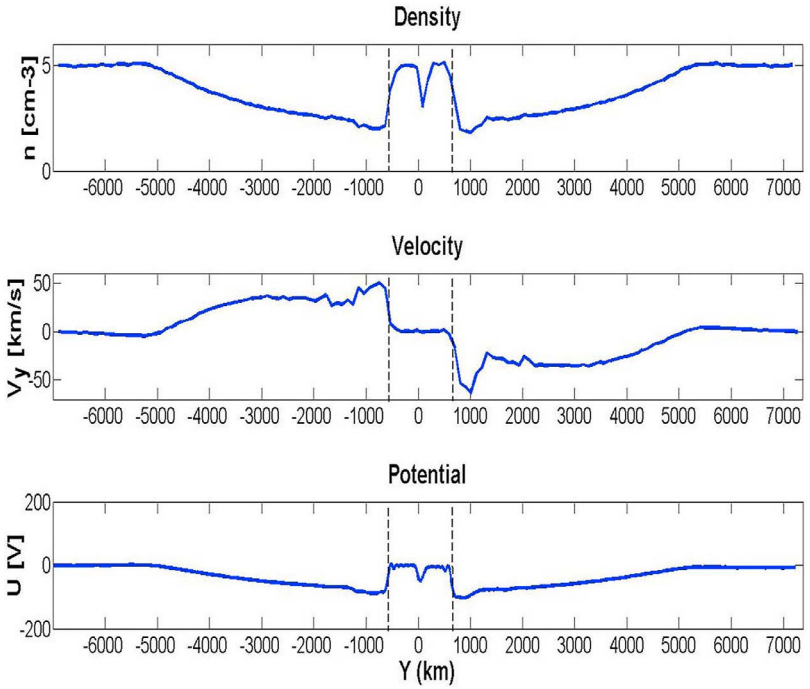

Figure 7. Profiles of plasma density, macroscopic velocity component V_y, and electric potential at $X = 16{,}000$ km.

$X = 12{,}500$ regions of standing plasma appear on both sides of the axis. These regions increase with the distance reaching ± 750 km from the axis. They correspond to the increase of the plasma density in the middle of the wake shown in Figure 1a.

[24] In a very narrow region, $Y < \pm 150$ km, two beams of protons with velocities ~ 90 km/s continue to exist till the end of simulation. Here, narrow minima of the plasma density (Figure 1a) and electric potential (Figure 1b) are observed.

[25] Figure 5 shows the velocity distribution functions at $X = 16{,}000$ km at three different positions along Y: -300 km, 0, and 300 km. Two beams ($\sim \pm 90$ km/s) exist at $Y = 0$, and at the distance of 300 km two slower beams (± 20 km/s and ∓ 40 km/s) almost overlap forming nearly Maxwellian velocity distribution.

[26] Change of the velocity distribution function along X-axis for given Y positions ($Y = 2800$ km, 1000 km, 300 km, and 0, denoted by dashed lines in Figure 1) is shown in Figure 6. For $Y = 2800$ km, the velocity distribution function remains unperturbed until $X = 6000$ km, when the outer Mach cone is crossed. Further down the wake, the velocity distribution function becomes shifted because of the plasma flow toward the wake axis. High-speed protons from the opposite sides of the wake are seen starting with $X \sim 10{,}000$ km. The line along $Y = 1000$ km starts inside the cavity and low-density plasma at rest is observed until $X = 2000$ km. Fast protons accelerated by the floating potential start to appear at this distance. The main injection of protons into the cavity starts at $X = 3000$ km. The flow velocity reduces from 140 km/s to 105 km/s at $X = 8000$ km and further remains constant. The flux of protons from the opposite side of the wake appears at $X = 5000$ km and two proton beams coexist for $X > 5000$ km without any significant interaction.

[27] For the line $Y = 300$ km, accelerated protons with $v = 220$ km/s appear at $X = 3000$ km, and the main plasma influx occurs at $X = 5500$ km. The oppositely directed beam of accelerated protons from the other side of the wake appears at $X = 4000$ km. The velocity of particles in this beam decreases with the distance, and two beams exhibiting some interaction exist until $X = 11{,}000$ km. At this distance, two-beam structure disappears, the plasma is at rest, and its density has increased.

[28] Along the wake axis, $Y = 0$, protons accelerated from both sides appear at $X = 4000$ km. At $X = 6000$ km the cavity collapses and the two beam distribution function becomes apparent. The relative velocity of the two beams reduced somewhat until $X = 8000$ km, and then remains practically unchanged exhibiting only quasiperiodic variations.

[29] The bottom row in Figure 4 ($X = 12{,}500$ km, 14,500 km and 16,000 km) show the existence of a discontinuity separating the region of plasma flow toward the wake center and the region of the plasma at rest with enhanced number density. Vertical dashed lines denote the location of the discontinuity. The macroscopic plasma parameters also have discontinuity at that location, as shown in Figure 7. Here the profiles of the density, macroscopic velocity, and electric potential along the Y-axis are given for $X = 16{,}000$ km. The dashed lines show the discontinuities positions on both sides of the wake axis.

[30] The simulated discontinuity has nonzero velocity component normal to the discontinuity surface and the plasma density and parallel velocity jump across the discontinuity. The discontinuity propagates with the velocity 41 km/s away from the tail axis. Behind the discontinuity the plasma is at rest. The incoming plasma velocity is 60 km/s in front of the discontinuity. Thus, in the discontinuity rest

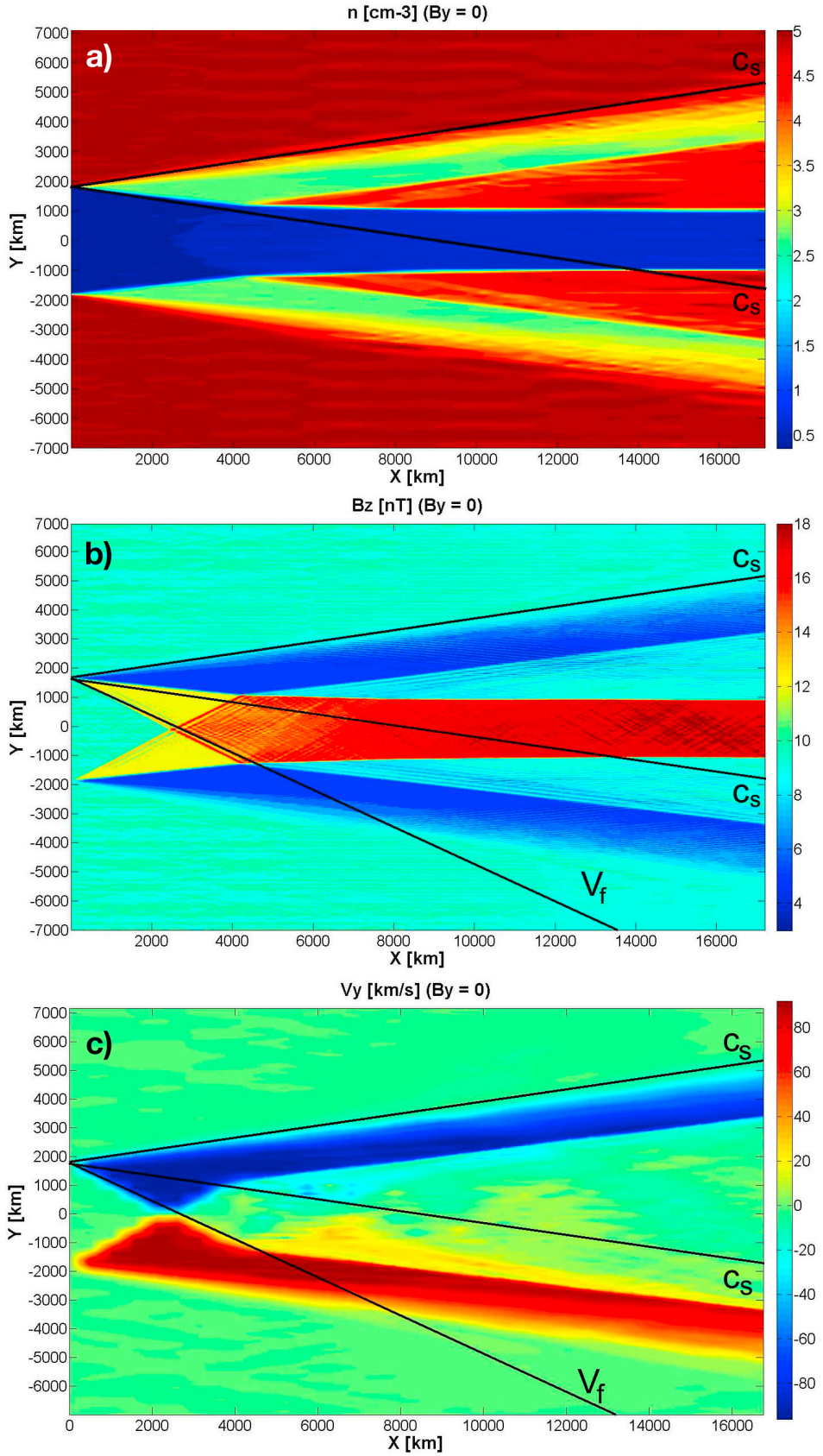

Figure 8. Distribution of the (a) number density, (b) magnetic field, and (c) plasma velocity component V_y in the wake for the case of expansion across the magnetic field. Solid lines denote the plasma expansion with ion-acoustic velocity c_s. Expansion with fast magnetosonic velocity V_f = 320 km/s is shown in Figures 8b and 8c.

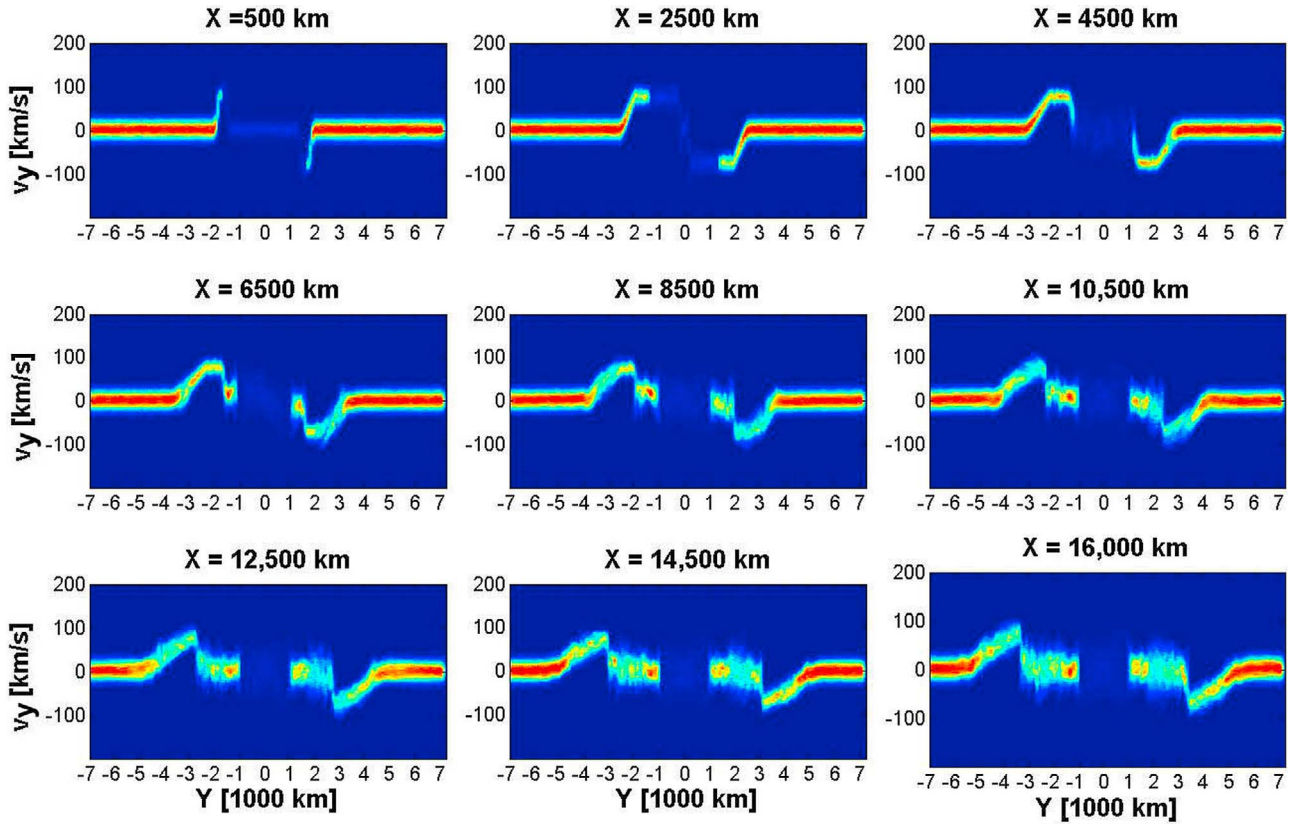

Figure 9. Distribution of protons in phase space ($y - v_y$) at 9 distances along the wake for the case of expansion across the magnetic field.

frame the plasma velocity is larger than c_s on the external side, and less than c_s behind the discontinuity. Therefore, this is collisionless slow shock wave [e.g., *Swift*, 1983].

3.2. Expansion Across the Magnetic Field ($B_x = B_y = 0$)

[31] For the case of plasma expansion across the magnetic field, the cavity containing the magnetic field is compressed by the magnetized plasma flow. Because of magnetic flux conservation the magnetic field in plasma-free cavity increases. The compression ceases when the magnetic pressure in the cavity reaches the value of the plasma thermal pressure in the unperturbed plasma flow. This is illustrated in Figure 8a showing the density distribution behind the obstacle. Contrary to the expansion along the magnetic field, the compression of the cavity as well as rarefaction wave expansion occur with the same velocity approximately equal to the ion-acoustic speed c_s, thus it can be described as the slow magnetosonic wave propagation. The pressure balance is reached at $X = 5000$ km where the cavity shape is changed and for $X > 5000$ km, the cavity cross-section remains constant. The cavity is surrounded by the region of enhanced plasma density that starts at the transition from collapsing to a constant cross-section as was predicted by *Michel* [1968]. The region of enhanced plasma density expands with the speed c_s.

[32] Magnetic field distribution and the velocity component V_y of plasma flow behind the obstacle are shown in Figures 8b and 8c. If the initial plasma density was zero immediately behind the obstacle, the magnetic field compression inside the cavity would propagate as an electromagnetic wave in vacuum with the speed of light c. However, the plasma density behind the obstacle was chosen $0.1n_0$ rather than zero (for stability of the numerical solution), and the compression inside the cavity occurs with fast magnetosonic speed $V_f = \sqrt{V_A^2 + c_s^2} = 320$ km/s as it is seen in the figure.

[33] Plasma flow toward the wake axis exists inside the rarefaction region. It vanishes rapidly at the boundary of the region of the enhanced plasma density.

[34] Proton velocity distribution functions in phase space (y, v_y) are shown in Figure 9 for $X = 500$ km, 2500 km, 4500 km, 6500 km, 8500 km, 10,500 km, 12,500 km, 14,500 km and 16,000 km.

[35] In contrast with the expansion along the magnetic field, there are no regions of two counterstreaming proton beams since the magnetic field prevents access of particles from one side of the obstacle to another side. As the magnetic field pressure in the cavity becomes stronger the plasma flow toward the axis of the wake decelerates (as seen for $X = 4500$ km). For the non-collapsing part of the cavity, the velocity at the cavity boundary is zero, the density increases, and the region of the plasma at rest with enhanced density expands with the distance from the obstacle. Thus we observe the typical pattern of plasma flow against a magnetic barrier. The velocity exhibits a discontinuity at the boundary of the dense plasma region so that the outer boundary of this region forms a shock wave.

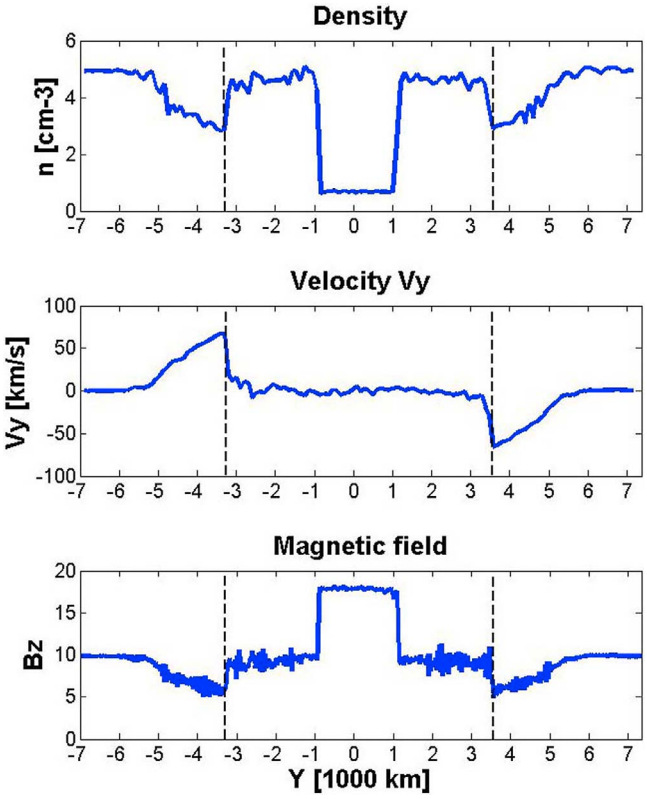

Figure 10. Profiles of plasma density, macroscopic velocity component V_y, and magnetic field at $X = 16{,}000$ km for the case of expansion across the magnetic field.

[36] Figure 10 shows the profiles of the density, macroscopic velocity and magnetic field along the Y-axis at $X = 16{,}000$ km. The quasi-perpendicular shock is observed in the case of plasma expansion across the magnetic field.

4. Conclusion

[37] The 1D hybrid simulation shows for the first time the appearance of the shock wave trailing the Moon in the distant wake, in agreement with past predictions [*Michel*, 1967]. The shock is produced by the interaction of oppositely directed proton beams in the plane containing solar wind velocity and interplanetary magnetic field vectors. In the direction across the magnetic field and the solar wind velocity, the shock results from the interaction of the plasma flow with the region of the enhanced magnetic field inside the cavity that plays the role of the magnetic barrier.

[38] The other main features of the solar wind interaction with the Moon known from observations and other numerical experiments are reproduced in this idealized 1D hybrid model: the formation of the cavity in the solar wind plasma and its collapse with ion-acoustic velocity, propagation of the rarefaction wave, negative charging of the cavity, existence of counterstreaming proton beams parallel to the magnetic field inside the cavity and in the rarefaction region, thus, validating our approach.

[39] For solar wind parameters ($T_i \ll T_e \sim 100$ eV, i.e., hot solar wind streams) used in the simulation, the shock starts to form at the approximate distance $\sim 3.5\ R_M$. The distance grows as the ratio of the IMF components B_y/B_x decreases reaching $7R_M$ for $B_y/B_x \sim 0.5$ (further decrease of the ratio causes very fast growth of the cavity length). The size of the region occupied by the shock is rather small. The distance between the quasi-parallel shock and the wake axis is only $0.4\ R_M$ at $X = 9\ R_M$. We repeated the simulations with lower electron temperatures ($T_e \sim 20$ eV) and found weakened shock formation trailing the moon at much greater distances. Therefore, in order to observe the trailing shock, a satellite should have a trajectory passing very close to the wake axis during the period of hot solar wind streams. In principle, ARTEMIS spacecrafts placed at L1 and L2 points of the Earth-Moon system [*Angelopoulos*, 2011] may cross the lunar wake sufficiently far downstream.

[40] **Acknowledgments.** LO would like to acknowledge support by NASA grant NNX10AC56G.

[41] Philippa Browning thanks the reviewers for their assistance in evaluating the paper.

References

Angelopoulos, V. (2011), The ARTEMIS Mission, *Space Sci. Rev.*, *165*, 3–25, doi:10.1007/s11214-010-9687-2.

Birch, P. C., and S. C. Chapman (2001), Detailed structure and dynamics in particle-in-cell simulations of the lunar wake, *Phys. Plasmas*, *8*, 4551–4559, doi:10.1063/1.1398570.

Bosqued, J. M., et al. (1996), Moon-solar wind interaction: First results from the WIND/3DP experiment, *Geophys. Res. Lett.*, *23*, 1259–1262, doi:10.1029/96GL00303.

Colburn, D. S., R. G. Currie, J. D. Mihalov, and C. P. Sonett (1967), Diamagnetic solar-wind cavity discovered behind Moon, *Science*, *158*, 1040–1042, doi:10.1126/science.158.3804.1040.

Farrell, W. M., M. L. Kaiser, J. T. Steinberg, and S. D. Bale (1998), A simple simulation of a plasma void: Applications to Wind observations of the lunar wake, *J. Geophys. Res.*, *103*, 23,653–23,660, doi:10.1029/97JA03717.

Feldman, W. C., J. R. Asbridge, S. J. Bame, M. D. Montgomery, and S. P. Gary (1975), Solar wind electrons, *J. Geophys. Res.*, *80*(31), 4181–4196, doi:10.1029/JA080i031p04181.

Halekas, J. S., R. P. Lin, and D. L. Mitchell (2005), Large negative lunar surface potentials in sunlight and shadow, *Geophys. Res. Lett.*, *32*, L09102, doi:10.1029/2005GL022627.

Halekas, J. S., Y. Saito, G. T. Delory, and W. M. Farrell (2011), New views of the lunar plasma environment, *Planet. Space Sci.*, *59*, 1681–1694, doi:10.1016/j.pss.2010.08.011.

Holmström, M., S. Fatemi, Y. Futaana, and H. Nilsson (2012), The interaction between the Moon and the solar wind, *Earth Planets Space*, *64*(2), 237–245, doi:10.5047/eps.2011.06.040.

Kallio, E. (2005), Formation of the lunar wake in quasi-neutral hybrid model, *Geophys. Res. Lett.*, *32*, L06107, doi:10.1029/2004GL021989.

Kimura, S., and T. Nakagawa (2008), Electromagnetic full particle simulation of the electric field structure around the moon and the lunar wake, *Earth Planets Space*, *60*, 591–599.

Kristoferson, L. (1969), Laboratory simulation experiment on solar wind interaction, *J. Geophys. Res.*, *74*, 906–908, doi:10.1029/JA074i003p00906.

Lipatov, A. S. (1976), Three-dimensional structure of the plasma wake of the Moon [in Russian], *Cosmic Res.*, *14*, 103–106.

Lipatov, A. S. (2002), *The Hybrid Multiscale Simulation Technology. An Introduction With Application to Astrophysical and Laboratory Plasmas*, Springer, Berlin.

Lipatov, A. S., J. F. Cooper, E. C. Sittler, and R. C. Hartle (2011), Effects of pickup ions on the solar wind near the lunar-like objects: 3D hybrid modeling, paper presented at EPSC-DPS Joint Meeting, ASTRIUM, Nantes, France.

Lyon, E. F., H. S. Bridge, and J. H. Binsack (1967), Explorer 35 plasma measurements in the vicinity of the Moon, *J. Geophys. Res.*, *72*, 6113–6117, doi:10.1029/JZ072i023p06113.

Michel, F. C. (1967), Shock wave trailing the moon, *J. Geophys. Res.*, *72*, 5508–5509, doi:10.1029/JZ072i021p05508.

Michel, F. C. (1968), Magnetic field structure behind the moon, *J. Geophys. Res.*, *73*, 1533–1542, doi:10.1029/JA073i005p01533.

Ness, N. F., K. W. Behannon, C. S. Seearce, and S. C. Cantarano (1967), Early results from the magnetic field experiment on Explorer 35, *J. Geophys. Res.*, *72*, 5769–5778, doi:10.1029/JZ072i023p05769.

Newbury, J. A., C. T. Russell, J. L. Phillips, and S. P. Gary (1998), Electron temperature in the ambient solar wind: Typical properties and a lower bound at 1 AU, *J. Geophys. Res.*, *103*(A5), 9553–9566, doi:10.1029/98JA00067.

Nishino, M. N., et al. (2009), Solar-wind proton access deep into the near-Moon wake, *Geophys. Res. Lett.*, *36*, L16103, doi:10.1029/2009GL039444.

Ofman, L., A. Viñas, and S. P. Gary (2001), Constraints on the O^{+5} anisotropy in the solar corona, *Astrophys. J.*, *547*, L175–L178, doi:10.1086/318900.

Ofman, L., M. Balichin, C. T. Russell, and M. Gedalin (2009), Collisionless relaxation of ion distributions downstream of laminar quasi-perpendicular shocks, *J. Geophys. Res.*, *114*, A09106, doi:10.1029/2009JA014365.

Ogilvie, K. W., et al. (1996), Observations of the lunar plasma wake from the WIND spacecraft on December 27, 1994, *Geophys. Res. Lett.*, *23*, 1255–1258, doi:10.1029/96GL01069.

Owen, C. J., et al. (1996), The lunar wake at 6.8RL: WIND magnetic field observations, *Geophys. Res. Lett.*, *23*, 1263–1266, doi:10.1029/96GL01354.

Podgorny, I. M., and Y. Andrijanov (1978), Simulation of the solar wind interaction with non-magnetic celestial bodies, *Planet. Space Sci.*, *26*, 99–109, doi:10.1016/0032-0633(78)90010-7.

Podgorny, I. M., E. M. Dubinin, and P. L. Israelevich (1980), Laboratory simulation of the induced magnetospheres of comets and Venus, *Moon Planets*, *23*, 323–338, doi:10.1007/BF00902047.

Samir, U., K. H. Wright Jr., and N. H. Stone (1983), The expansion of a plasma into a vacuum: Basic phenomena and processes and applications to space plasma physics, *Rev. Geophys.*, *21*, 1631–1646, doi:10.1029/RG021i007p01631.

Sittler, E. C., Jr., and L. F. Burlaga (1998), Electron temperatures within magnetic clouds between 2 and 4 AU: Voyager 2 observations, *J. Geophys. Res.*, *103*(A8), 17,447–17,454, doi:10.1029/98JA01289.

Swift, D. W. (1983), On the structure of the magnetic slow switch-off shock, *J. Geophys. Res.*, *88*, 5685–5691, doi:10.1029/JA088iA07p05685.

Wambecq, A. (1978), Rational Runge-Kutta methods for solving systems of ordinary differential equations, *Computing*, *20*, 333–342, doi:10.1007/BF02252381.

Wang, Y.-C., J. Müller, W.-H. Ip, and U. Motschmann (2011), A 3D hybrid simulation study of the electromagnetic field distributions in the lunar wake, *Icarus*, *216*, 415–425, doi:10.1016/j.icarus.2011.09.021.

Wiehle, S., et al. (2011), First lunar wake passage of ARTEMIS: Discrimination of wake effects and solar wind fluctuations by 3D hybrid simulations, *Planet. Space Sci.*, *59*, 661–671, doi:10.1016/j.pss.2011.01.012.

Winske, D., and N. Omidi (1993), Hybrid codes: Methods and applications, in *Computer Space Plasma Physics: Simulation Techniques and Software*, edited by H. Matsumoto and Y. Omura, 103–160, Terra Sci., Tokyo.

Wolf, R. A. (1968), Solar wind flow behind the moon, *J. Geophys. Res.*, *73*, 4281–4289, doi:10.1029/JA073i013p04281.